Structure and lipid dynamics in the *A. baumannii* maintenance of lipid asymmetry (MLA) inner membrane complex

Daniel Mann[1,&], Junping Fan[3,%], Daniel P. Farrell[4], Kamolrat Somboon[5], Andrew Muenks[4], Svetomir B. Tzokov[1], Syma Khalid[5] ,Frank Dimaio[4], Samuel I. Miller[3,4,6], Julien R. C. Bergeron[1,2]*

[1] Department of Molecular Biology and Biotechnology, The University of Sheffield, Sheffield, United Kingdom

[2] Randall Division of Cell and Molecular Biophysics, King's College London, London, UK

[3] Department of Microbiology, The University of Washington, Seattle, USA

[4] Department of Biochemistry, The University of Washington, Seattle, USA

[5] Department of Chemistry, University of Southampton, Southampton, UK

[6] Department of Genetics, The University of Washington, Seattle, USA

[&] Current address: Ernst-Ruska-Centre 3, Forschungszentrum Jülich, Germany

[%] Current address: Department of Pharmacology, The University of Washington, Seattle, USA

*Correspondence to: julien.bergeron@kcl.ac.uk

Abstract

Multi-resistant bacteria are a major threat in modern medicine. The gram-negative coccobacillus *Acinetobacter baumannii* currently leads the WHO list of pathogens in critical need for new therapeutic development. The maintenance of lipid asymmetry (MLA) protein complex is one of the core machineries that transport lipids from/to the outer membrane in gram-negative bacteria. It also contributes to broad-range antibiotic resistance in several pathogens, most prominently in *A. baumannii*. Nonetheless, the molecular details of its role in lipid transport has remained largely elusive.

Here, we report the cryo-EM structures of the core MLA complex, MlaBDEF, from the pathogen *A. baumannii*, in the apo-, ATP- and ADB-bound states. These structures reveal multiple lipid binding sites, in the cytosolic and periplasmic side of the complex. Molecular dynamics simulations suggest their potential trajectory across the

33 membrane. Collectively with the recently-reported structures of the *E.coli* orthologue,
34 these data also allows us to propose a molecular mechanism of lipid transport by the
35 MLA system.

36 ## Introduction:

37 Gram-negative bacteria are enveloped by two lipid bilayers, separated by the
38 periplasmic space containing the peptidoglycan cell wall. The two membranes have
39 distinct lipid compositions: The inner membrane (IM) consists of glycerophospholipids,
40 with both leaflets having similar compositions, while the outer membrane (OM) is
41 asymmetric, with an outer leaflet of lipopolysaccharides (LPS) and an inner leaflet of
42 glycerophospholipids (1) (Fig. 1 A). This lipid gradient, depicting the first and most
43 important permeation barrier is maintained by several machineries, including YebT,
44 PqiB, and the multicomponent MLA system (2, 3), which consists of MlaA present in
45 the OM, the shuttle MlaC in the periplasmic space, and the MlaBDEF ABC transporter
46 system in the IM (Fig. 1 A). The structure of some of these components have previously
47 been solved: the OM protein MlaA, which was found to form a stable complex with
48 outer membrane porins OmpF and OmpC (4, 5), and the periplasmic protein MlaC
49 revealing a hydrophobic pocket for direct lipid transport through the periplasm (2, 6).
50 Low-resolution cryo-EM maps of the MlaBDEF core complex, from *Escherichia coli*
51 ($MlaBDEF_{ec}$)(2) and *Acinetobacter baumannii* ($MlaBDEF_{ab}$) (7) have also been
52 reported, and revealed the overall architecture of the complex, but did not allow to
53 elucidate the molecular details of lipid binding and transport. Opinions about the
54 directionality of lipid transport by the MLA system have been highly controversial, with
55 initial reports suggesting that it recycles lipids from the OM to the IM (2, 8, 9), but recent
56 results (7, 10, 11) indicated that it might exports glycerophospholipids to the outer
57 membrane.

58 In this study, we report the structure of the $MlaBDEF_{ab}$ complex in detergent, in three
59 nucleotide states, by single-particle cryo-EM. We also performed molecular dynamics
60 simulations to gain insights into the dynamics of lipids within their observed binding
61 sites. Collectively, this provides important new insights in the mechanism of lipid
62 transport by the MLA system, and about the characterization of membrane proteins in
63 detergent.

64

Results:

Structure of MlaBDEF$_{ab}$

We had previously reported the purification of MlaBDEF$_{ab}$ in the presence of the detergent n-dodecyl β-D-maltoside (DDM), and its structure to ~ 8 Å, by single-particle cryo-EM, from data collected on a side-entry 200kV microscope (7). In order to improve the resolution of this structure, we collected a dataset of the same complex, in the presence of the non-hydrolizable ATP analogue App-NHp, using a state-of-the-art Titan Krios instrument. Using this better and larger dataset, we were able to refine the structure to ~ 3.9 Å resolution (Fig. 1B, Suppl. Fig. 1, Table 1). This map allowed us to build a *de-novo* atomic model using Rosetta (12) (See Materials and Methods for details).

As shown of figures 1B, and 1C, the transmembrane multiprotein complex features a 6-fold symmetric assembly of MlaD, with the C-terminal helix forming a basket in the periplasmic space (Fig. 1D), and the N-terminal helix spanning the inner membrane (Fig. 1C). The N-terminal TM helices of MlaD are wrapped around the two MlaE molecules in the membrane, with three MlaD helices interacting asymmetrically with one MlaE, as reported previously (7). Intriguingly, while MlaE was predicted to have 6 TM helices, we observe that TM1 does not traverse the membrane, but is monotropically embedded in the inner leaflet, a feature similar to the G5G8 human sterol exporter (13), suggesting similar mechanisms between these complexes, and further supporting the MLA system as a lipid exporter. On the cytosolic side, MlaE is anchored into the ATPase MlaF via the coupling helix situated between TM3 and TM4 (Fig. 1), again similar to the G5G8 sterol exporter complex. MlaF is bound to MlaB away from the nucleotide binding site, similar to the recently-reported *E.coli* MlaBF structure (14), with C-termini of MlaF binding the opposing MlaB subunit by a “handshake” mode (Fig. 1E). We note, however, that particle classification demonstrated that only ~50% of the particles included MlaB bound to both MlaF, leaving the other 50% bound to only one copy of MlaB (Suppl. Fig. 2). Dual binding of MlaB did not introduce major structural alterations at the detected resolution, and this observation may correspond to a regulatory role for MlaB or could be due to complex disassembly during sample preparation.

97 **Lipids spontaneously bind into pockets of cytoplasmic MlaBDEF$_{ab}$**

98 In the cryo-EM derived map of MlaBDEF$_{ab}$, observed well-defined density in the pocket
99 formed between the MlaE TM1, and two MlaD helices, within the inner leaflet of the
100 lipid bilayer (Fig 2 A-C), which could not be interpreted by protein atoms. We also
101 observed that this pocket is coated by cationic residues, mainly Arg14, Arg47 and
102 Arg234 of MlaE, forming a charged pocket that might attract a lipid head group (Fig.
103 2D). This observation prompted us to propose that this density corresponds to
104 detergent molecules bound to the complex. As the sample was solubilized in DDM,
105 this density is most likely occupied by the maltoside ring, with the flexible hydrophobic
106 chains extending up into an apolar region of MlaE. In order to confirm if the observed
107 density was consistent with lipid positioning, we performed molecular dynamics
108 simulations with unoccupied binding pockets as starting structures and observed rapid
109 incorporation of bulk lipids during equilibration (Fig. 2 E). Newly bound lipids remained
110 stably bound during 500 ns production runs (Fig. 2 F), depicting a reasonable first step
111 in lipid export. This result is consistent with the position of lipid molecules within this
112 region of the MlaBDEF$_{ab}$ complex.

113

114 **Lipids bind into the periplasmic basket and partially flip**

115 The periplasmic region of MlaBDEF$_{ab}$ consists mainly of hexameric MlaD forming a
116 basket shape (Fig. 1). Similar to other MCE domain proteins (15), MlaD consists of a
117 central beta sheet motif with a central pore loop that is formed by hydrophobic
118 Leu153/Leu154 in the center of the C6 symmetric complex (Fig. 3 A). We observed
119 that in our map, unattributed density was present between the central pore loops, as
120 well as in the central pore (Fig. 3 A). Importantly, this density is not an artifact of the 6-
121 fold symmetry, as it is also resolved when no symmetry was applied during the
122 reconstruction. The presence of lipid molecules in very similar positions were
123 previously reported in the MCE protein YebT (16), which prompted us to postulate that
124 this unattributed density on the MlaD periplasmic region also corresponds to detergent
125 molecules. Of note, the basket region has previously been proposed to form the
126 binding site for the periplasmic carrier protein MlaC (4), suggesting that lipids are
127 extracted from this position upon MlaC binding, consistent with the interpretation that
128 these regions of the map correspond to lipid molecules.

129 Because of this likely important role of lipid dynamics for this region, we next performed
130 3D variability analysis (17), to identify molecular motions in the MlaD crown. As shown
131 on Suppl. movies 1 and 2, this analysis revealed that the 6x MlaD crown can be
132 translated and rotated against the MlaBEF transmembrane part, which may play a role
133 in the lipid transport mechanism. Incidentally, this dynamic property likely also limits
134 the achievable resolution for this region of the map.

135 To further investigate the dynamic properties of the lipids present in the MlaD basket,
136 we subjected them to molecular dynamics simulations. As shown on Figures 3 B-C,
137 we observed that the peripheral lipids are rather stable during the course of the
138 simulation. In contrast, the central lipid undergoes a significant motion within 150 ns of
139 the trajectory. Remarkably, during this motion, we observed lipid flipping (Figure 3 D),
140 with the head group which was modeled away from the central pore operating an
141 almost 180°, with the polar group buried within the MlaE transporter. This observation
142 likely indicates that we had initially build the lipid in the wrong orientation, and highlights
143 the importance of properly modeling lipid molecules, especially at the intermediate
144 resolution such as that of our $MlaBDEF_{ab}$ map. In addition, this demonstrates the
145 presence of a large hydrophobic pocket at the MlaD-MlaE interface, which could
146 correspond to the channel for lipid transport.

147

148 **Nucleotide binding occurs at the interface of MlaE, MlaF and MlaD**

149 As indicated above, our structure of $MlaBDEF_{ab}$ was determined in the presence of the
150 non-hydrolizable ATP analogue AppNHp. Accordingly, we observed clear density of
151 the nucleotide and Magnesium, within the MlaF binding pocket (Fig. 4A). The
152 nucleotide links the ATPase subunits with the lipid transport domains at the interface
153 of MlaF, MlaE and the N-terminus of MlaD. The resolution was sufficient to map the
154 phosphate binding regions like Walker-A motif around Lys55 of MlaF, as well as
155 binding of the γ-Phosphate by Ser51 and His211 (H-loop). The Mg^{2+}-ion is coordinated
156 by the Walker-B motif around Asp177 (Fig. 4A) and adenosine ring binding is achieved
157 through Arg26 in the A-loop. As revealed in the previously-reported low-resolution map
158 (7), the position of MlaF suggest that the complex is in the substrate-bound
159 conformation.

160 In order to identify structural changes in the complex associated with ATP binding and
161 hydrolysis, we next determined the structure of $MlaBDEF_{ab}$ without nucleotide (Suppl.
162 Fig. 3), and with ADP (Suppl. Fig. 4). As shown on Figure 4A-C, we obtained both
163 structures, to ~4.2 Å and ~ 4.4 A, respectively (Table 1). We note that in spite of the
164 nominar global resolution, the map for the complex bound to ADP possesses features
165 largely similar to that of the complex bound to AppNHp. In contrast, the map of the apo
166 complex is less well resolved, in particular with most TM helices being mostly
167 featureless. This suggests that nucleotide binding stabilizes the overall architecture of
168 the $MlaBDEF_{ab}$ complex.

169 Nonetheless, we note that the overlay of the $MlaBDEF_{ab}$ maps in the apo, AppNHp-
170 bound, and ADP-bound states show no major structural changes in any of the complex
171 components, other than the nucleotide binding site (Fig. 4D). This indicates that in spite
172 of the nucleotides being bound to the ATPase domain, under the conditions used this
173 is not sufficient to trigger the activation of the channel opening.

174

175 **Discussion:**

176 While this manuscript was under review, three independent groups released the
177 structure of the *Escherichia coli* MlaBDEF complex ($MlaBDEF_{ec}$), in a range of
178 nucleotide states and with various solubilization approaches (18–20).

179 Comparison of the $MlaBDEF_{ec}$ structure (PDB-ID 7CH0, 7CGN), determined in lipid
180 nanodiscs, and the $MlaBDEF_{ab}$ structure (this study), determined in DDM, reveals a
181 ~10 Ang movement of the MlaD TM helices, accompanied by a ~30° tilt of the MlaE
182 N-terminal helix (Fig. 5 A). This movement narrows the cytoplasmic allocrit binding
183 pocket significantly (Fig. 5 A, red circles). A structural flexibility like this would allow
184 adjustment of MlaBDEF for allocrits with varying sizes. However, as lateral pressure in
185 the membrane plane of a detergent micelle is not comparable to a lipid nanodisc,
186 differences in sample preparation can also cause movement of this hinge.
187 Furthermore, although the MLA system is conserved in gram-negative bacteria, the
188 sequence identity between the $MlaBDEF_{ab}$ $MlaBDEF_{ec}$ proteins is around 30-40%
189 identity (depending on the protein), and it is therefore possible that the differences
190 observed between the two structures correspond to variability between bacterial
191 species.

192

193 Significantly, in one of the aforementioned studies, two ATP-bound conformational
194 states were observed for MlaBDEF$_{ec}$: a more open conformation ("*tall state*") and a
195 tightly bound conformation ("*close state*"), with a significantly shifted nucleotide
196 position. The nucleotide position in MlaBDEF$_{ab}$ in detergent resembles the *tall state*
197 with an open conformation of MlaF (Fig. 5 B-C).

198 We also note that the lipid binding pockets observed in our MlaBDEF$_{ab}$ structures are
199 also confirmed in the MlaBDEF$_{ec}$ structures, notably the lipids found between the MlaD
200 TM and the N-terminal helix of MlaE (20), and the lipid present in the central cavity
201 (18–20). For the later, different exact lipid positions are observed depending on the
202 state and study, but they are largely consistent with the lipid position obtained in the
203 MD simulation, with the charged group buried at the MlaE-MlaD interface. In contrast,
204 our map is the only one with clear lipid density at the interface between MlaD molecules
205 in the periplasmic site; this could correspond to species specificity, or could be an
206 artifact of the use of detergent for structure determination.

207 In the light of the multiple structures now available, the structures of MlaBDEF$_{ab}$
208 reported here support a mechanism for lipid export as summarized in Figure 6. We
209 observe lipids binding to the inner lipid binding pocket; this region is likely flexible and
210 can possibly adapt to the size of the allocrit. MlaE is in very close proximity to ATP in
211 the closed conformation, possibly describing an additional regulatory mechanism in *A.*
212 *baumannii*. Structures of MlaBDEF$_{ec}$ also showed a large-scale structural alteration
213 upon tight ATP binding (20) that might be restrained due to the detergent environment
214 in our experiments. We could furthermore observe a central lipid binding cite in the
215 periplasmic basket region of MlaD that could partially flip into the central channel of
216 MlaE during the course of our MD simulation. Nonetheless, neither our structures of
217 MlaBDEF$_{ab}$ nor the aforementioned MlaBDEF$_{ec}$ could resolve allocrit transition
218 between the cytoplasmic lipid binding pocket and the central channel. Similarly, allocrit
219 transport from MlaBDEF to MlaC remains elusive.

220 It should be emphasized that the structural studies reported here support an
221 anteretrograde direction for lipid transport, as supported by our previous biochemical
222 data in *A. baumannii* (19) as well as other studies in *E. coli* (11, 19, 20). Nonetheless,
223 other assays point towards a retrograde directionality (18, 21), and the current
224 structures do not conclusively preclude this. Further structural analyses, in particular

225 in complex with the periplasmic carrier MlaC, will be required to definitely resolve this
226 controversy.

227

228 ## Materials & Methods:

229 **MlaBDEF$_{ab}$ protein expression and purification**

230 The expression and purification of MlaBDEF$_{ab}$ has been described previously (7).
231 Briefly, the plasmid was transformed into *Escherichia coli* BL21 DE3 cells and grown
232 at 37°C until the cell density reached OD(600nm) = 1.0. The temperature was reduced
233 to 20°C before induction with 1 mM isopropyl β-D-thiogalactoside (IPTG) and
234 incubation overnight. Cells were harvested using centrifugation at 5000 x g and
235 resuspended in ice-cold buffer A (20 mM Tris-HCl (pH 8.0), 150 mM NaCl, 5% (v/v)
236 glycerol) before disruption in an ultrasonicator on ice (6 cycles; 60s run, 30s cooldown).
237 Cell debris was centrifuged down at 17,000 x g for 10 min and the supernatant was
238 centrifuged at 100,000 x g for 1h. This pellet was resuspended by gentle stirring in
239 Buffer A supplemented with 1% (w/v) dodecyl-β-d-maltopyranoside (DDM) at 7°C for
240 1 h. After another centrifugation step at 100,000 x g for 30 min the supernatant was
241 applied to a 5 ml Ni-NTA superflow column (GE Healthsciences) that was previously
242 equilibrated with ddH_2O and buffer A supplemented with 20 mM imidazole and 0.025%
243 (w/v) DDM. The column was washed with buffer A supplemented with 20 mM imidazole
244 and 0.025% (w/v) DDM before elution with buffer A supplemented with 300 mM
245 imidazole and 0.025 % (w/v) DDM was performed. The elute was concentrated to 5 ml
246 and applied to a gel filtration run on a 16-600 HiLoad Superdex 200 pg column (GE
247 Healthcare), preequilibrated with 20 mM Hepes (pH 7.0), 150 mM NaCl, 0.025% (w/v)
248 DDM. Peak fractions were collected, purest fractions were selected using SDS-PAGE
249 and concentrated to 5 mg/ml.

250

251 **CryoEM sample preparation, data acquisition and image processing**

252 4 µl freshly purified 5 mg/ml MlaBDEF$_{ab}$ in 20 mM Hepes (pH 7.0), 150 mM NaCl,
253 0.025% (w/v) DDM was applied on 30s freshly glow discharged 300 mesh Quantifoil
254 R2/2 grids, blotted for 3.5 s in a Leica EM-GP plunge freezer at 80% humidity and 4°C,
255 before getting plunged into liquid ethane at -170 °C. For investigation of the AppNHp

256 and ADP states, the protein was mixed 1:1 with 20 mM of the corresponding nucleotide
257 in 50 mM Hepes (pH 8.0), 150 mM NaCl, 0.025 % (w/v) DDM buffer and incubated for
258 60 min on ice prior to grid preparation.

259 Micrographs of MlaBDEF$_{ab}$-AppNHp were recorded on a 300 kV Titan Krios
260 microscope with a Gatan K2 Summit detector in counting mode. 2557 movies were
261 recorded with a pixel size of 1.07 Ang in 47 frames with 1e$^-$/Ang^2/frame. 1901 movies
262 of MlaBDEF$_{ab}$-ADP were recorded on the same instrument with a total dose of 40 e$^-$
263 /Ang^2. The MlaBDEF$_{ab}$ apo dataset was recorded on a 300 KV Titan Krios equipped
264 with a Gatan K3 bioquantum detector. 4737 micrographs with a pixel size of 0.41 Ang
265 were recorded with a total dose of 40 e$^-$/Ang^2 in 50 frames. Data processing was
266 performed in CryoSPARC v2.14.2 (see Suppl. Fig. 1 and 3 for details). Raw images of
267 the MlaBDEF$_{ab}$-AppNHp dataset are publicly available under EMPIAR-10425.
268 Sharpened maps in C2, C1 and C6 symmetry, masks and half-maps of MlaBDEF$_{ab}$-
269 AppNHp, ADP and apo are publicly available under EMD-11082, EMD-11083 and
270 EMD-11084, respectively.

271

272 **Model building**

273 The structural model of MlaBDEF$_{ab}$ was manually built into the high-resolved regions
274 of the MlaBDEF$_{ab}$-AppNHp map using Coot. Computational intervention was required
275 to build residues 4-38, and 94-134 of MlaD, as well as refine the AppNHp binding site
276 of MlaF. RosettaES (12) was used to model residues 4-38 for each of the 6 MlaD
277 subunits using the manually built model as the starting point. Residues 94-134 were
278 first modeled with Rosetta *Ab-initio* (22) which yielded a tightly converged ensemble
279 with a 2-helix topology. The top scoring model from the *Ab-initio* predictions was
280 unambiguously docked into the corresponding density for each of the MlaD subunits
281 using UCSF Chimera (23). Loops were completed and the entire MlaD crown refined
282 using RosettaCM (24) with the context of the cryoEM density. To refine the AppNHp
283 binding site of MlaF we first used RosettaCM to hybridize the manually built model with
284 the homologous structures of (3fvq, chain A), and (4ki0, chain B) in the cryoEM density.
285 Then using homology models and the unexplained density as a guide, a modified
286 version of the rosetta protocol GALigandDock (unpublished) that uses the cryoEM data
287 to drive sampling was used to dock the AppNHp molecule. As input to the protocol, a
288 mol2 file of AppNHp was modified using openbabel (v. 2.4.1) (25) to add hydrogens,

289 charges were assigned with the AM1-BCC charge method in antechamber (26) and a
290 params file was generated with the script
291 main/source/scripts/python/public/generic_potential/mol2genparams.py which is
292 distributed with Rosetta. Finally, the entire complex was refined using RosettaCM, and
293 Magnesium atoms were added by incorporating distance and angle constraints
294 between the Mg atoms and the AppNHp oxygens on the β and γ phosphates during
295 the final minimization. ISOLDE in ChimeraX was used to manually correct for modeling
296 errors. Phenix.real.space.refine was used for refinement and validation. As shown on
297 Suppl. Fig. 5 and 6, the resoluting model has an excellent fit to the map density, with
298 clear fit of the side-chains in particular for the TM helices of MlaE and MlaD, which
299 were critical for determining their registry. We note nonetheless that the TM for one of
300 the MlaD molecules is mostly featureless (orange in suppl. Fig. 6), in which case we
301 relied on the other two copies to position the helix in the density. The $MlaBDEF_{ab}$-
302 AppNHp model is publicly available under PDB-6Z5U.

303

304 **Molecular dynamics system preparation**

305 The $MlaBDEF_{ab}$ structure was completed by adding the missing residues using
306 Modeller 9.23 (http://salilab.org/modeller/)(27, 28). A system, having the completed
307 protein structure embedded in an inner *E.coli* innermembrane, was generated with the
308 CHARMM GUI web interface(29–35) to have dimension of approximately 21 × 21 ×
309 18 nm in xyz dimension. The innermembrane composition was based on previous
310 atomistic simulations studies(36): 75% 1-palmitoyl-2-oleoyl-sn-glycero-3-
311 phosphoethanolamine (POPE), 20% 1-palmitoyl-2-oleoyl-sn-glycero-3-
312 phosphoglycerol (POPG) and 5% 1′,3′-bis[1,2-dioleoyl-sn-glycerol-3-phospho-]-sn-
313 glycerol (Cardiolipin). To relax any steric conflicts within the system generated during
314 set up, energy minimization of 5000 steps was performed on the starting conformation
315 using the steepest descent method. An equilibration procedure followed in which the
316 protein was subjected to position restraints with different force constant. The full
317 equilibration protocol is shown in Suppl. Table 1. Fatty acid molecules were placed
318 around the entrance of MLA using Visual Molecular Dynamics (VMD)(37).

319

320 **Equilibrium molecular dynamics simulations**

All simulations were carried out with GROMACS 2019.6(38) version (www.gromacs.org) and CHARMM36(39) forcefield. For the nonbonded interactions and the short-range electrostatics cut offs of 1.2 nm was applied to the system with the potential shift Verlet cut off scheme, whereas the long-range electrostatic interactions were treated using the Particle Mesh Ewald (PME) method(40). All atoms were constrained using the LINCS algorithm(41) to allow the time step of 2 fs. The desired temperature at either 310 K or 323 K was controlled with Nose-hoover thermostat(42, 43) (1.0 ps coupling constant). The pressure was maintained at 1 atm using the Parrinello-Rahman(44) semi-isotropic barostat with a coupling constant of 1.0 ps. Equilibrium MD systems were performed with two repeats. Each repeat was run with different initial velocities. The summary of all production runs is shown in Suppl. Table 2. The results were analysed using built-in function in GROMACS package. Molecular graphic pictures were prepared using VMD.

Acknowledgments:

We are thankful for financial support through BBSRC project BB/R019061/1. We acknowledge Diamond Light Source for access and support of the cryo-EM facilities at the UK's national Electron Bio-imaging Centre (eBIC) [under proposal EM-19832]. We thank Emma Hasketh and Rebecca Thompson from the Astbury Centre for Structural Molecular Biology Leeds for support during measurements. We acknowledge support from LonCEM, King's College London during measurements. The University of Sheffield FoS cryo-EM facility was used for grid preparation and optimization. We are grateful to Justin Kollman for help with the initial stages of this project.

1. Zhang, Y.-M., and Rock, C. O. (2008) Membrane lipid homeostasis in bacteria. *Nat. Rev. Microbiol.* **6**, 222–233

2. Ekiert, D. C., Bhabha, G., Isom, G. L., Greenan, G., Ovchinnikov, S., Henderson, I. R., Cox, J. S., and Vale, R. D. (2017) Architectures of Lipid Transport Systems for the Bacterial Outer Membrane. *Cell*. **169**, 273-285.e17

3. Isom, G. L., Coudray, N., MacRae, M. R., McManus, C. T., Ekiert, D. C., and Bhabha, G. (2020) LetB Structure Reveals a Tunnel for Lipid Transport across the Bacterial Envelope. *Cell*. **181**, 653-664.e19

4. Abellón-Ruiz, J., Kaptan, S. S., Baslé, A., Claudi, B., Bumann, D., Kleinekathöfer, U., and van den Berg, B. (2017) Structural basis for maintenance of bacterial outer membrane lipid asymmetry. *Nat. Microbiol.* **2**, 1616–1623

5. Yeow, J., Tan, K. W., Holdbrook, D. A., Chong, Z.-S., Marzinek, J. K., Bond, P. J., and Chng, S.-S. (2018) The architecture of the OmpC–MlaA complex sheds light on the maintenance of outer membrane lipid asymmetry in Escherichia coli. *J. Biol. Chem.* **293**, 11325–11340

6. Huang, Y.-M. M., Miao, Y., Munguia, J., Lin, L., Nizet, V., and McCammon, J. A. (2016) Molecular dynamic study of MlaC protein in Gram-negative bacteria: conformational flexibility, solvent effect and protein-phospholipid binding. *Protein Sci. Publ. Protein Soc.* **25**, 1430–1437

7. Kamischke, C., Fan, J., Bergeron, J., Kulasekara, H. D., Dalebroux, Z. D., Burrell, A., Kollman, J. M., and Miller, S. I. (2019) The Acinetobacter baumannii Mla system and glycerophospholipid transport to the outer membrane. *eLife*. **8**, e40171

8. Malinverni, J. C., and Silhavy, T. J. (2009) An ABC transport system that maintains lipid asymmetry in the gram-negative outer membrane. *Proc. Natl. Acad. Sci. U. S. A.* **106**, 8009–8014

9. Thong, S., Ercan, B., Torta, F., Fong, Z. Y., Wong, H. Y. A., Wenk, M. R., and Chng, S.-S. (2016) Defining key roles for auxiliary proteins in an ABC transporter that maintains bacterial outer membrane lipid asymmetry. *eLife*. **5**, e19042

10. Hughes, G. W., Hall, S. C. L., Laxton, C. S., Sridhar, P., Mahadi, A. H., Hatton, C., Piggot, T. J., Wotherspoon, P. J., Leney, A. C., Ward, D. G., Jamshad, M., Spana, V., Cadby, I. T., Harding, C., Isom, G. L., Bryant, J. A., Parr, R. J., Yakub, Y., Jeeves, M., Huber, D., Henderson, I. R., Clifton, L. A., Lovering, A. L., and Knowles, T. J. (2019) Evidence for phospholipid export from the bacterial inner membrane by the Mla ABC transport system. *Nat. Microbiol.* **4**, 1692–1705

11. Hughes, G. W., Sridhar, P., Nestorow, S. A., Wotherspoon, P. J., Cooper, B. F., and Knowles, T. J. (2020) MlaFEDB displays flippase activity to promote phospholipid transport towards the outer membrane of Gram-negative bacteria. *bioRxiv*. 10.1101/2020.06.06.138008

12. Frenz, B., Walls, A. C., Egelman, E. H., Veesler, D., and DiMaio, F. (2017) RosettaES: a sampling strategy enabling automated interpretation of difficult cryo-EM

388 maps. *Nat. Methods*. **14**, 797–800

389 13. Lee, J.-Y., Kinch, L. N., Borek, D. M., Wang, J., Wang, J., Urbatsch, I. L., Xie,
390 X.-S., Grishin, N. V., Cohen, J. C., Otwinowski, Z., Hobbs, H. H., and Rosenbaum, D.
391 M. (2016) Crystal structure of the human sterol transporter ABCG5/ABCG8. *Nature*.
392 **533**, 561–564

393 14. Kolich, L., Chang, Y-T., Coudray, N., Giacometti, S. I., MacRae, M. R., Isom,
394 G. L., Teran, E. M., Bhabha, G., and Ekiert, D. C. (2020) Structure of MlaFB
395 uncovers novel mechanisms of ABC transporter regulation. bioRxiv
396 10.1101/2020.04.27.064196v1.full

397 15. Isom, G. L., Davies, N. J., Chong, Z.-S., Bryant, J. A., Jamshad, M., Sharif, M.,
398 Cunningham, A. F., Knowles, T. J., Chng, S.-S., Cole, J. A., and Henderson, I. R.
399 (2017) MCE domain proteins: conserved inner membrane lipid-binding proteins
400 required for outer membrane homeostasis. *Sci. Rep.* **7**, 1–12

401 16. Liu, C., Ma, J., Wang, J., Wang, H., and Zhang, L. (2020) Cryo-EM Structure
402 of a Bacterial Lipid Transporter YebT. *J. Mol. Biol.* **432**, 1008–1019

403 17. Punjani, A., and Fleet, D. J. (2020) 3D Variability Analysis: Directly resolving
404 continuous flexibility and discrete heterogeneity from single particle cryo-EM images.
405 *bioRxiv*. 10.1101/2020.04.08.032466

406 18. Tang, X., Chang, S., Qiao, W., Luo, Q., Chen, Y., Jia, Z., Coleman, J., Zhang,
407 K., Wang, T., Zhang, Z., Zhang, C., Zhu, X., Wei, X., Dong, C., Zhang, X., and Dong,
408 H. (2020) Structural insight into outer membrane asymmetry maintenance of Gram-
409 negative bacteria by the phospholipid transporter MlaFEDB. *bioRxiv*.
410 10.1101/2020.06.04.133611

411 19. Coudray, N., Isom, G. L., MacRae, M. R., Saiduddin, M. N., Bhabha, G., and
412 Ekiert, D. C. (2020) *Structure of bacterial phospholipid transporter MlaFEDB with*
413 *substrate bound*, BioRXiv, 10.1101/2020.06.02.129247

414 20. Chi, X., Fan, Q., Zhang, Y., Liang, K., Wan, L., Zhou, Q., and Li, Y. (2020)
415 Structural mechanism of phospholipids translocation by MlaFEDB complex. *Cell Res.*
416 10.1038/s41422-020-00404-6

417 21. Powers, M. J., Simpson, B. W., and Trent, M. S. (2020) The Mla pathway in
418 Acinetobacter baumannii has no demonstrable role in anterograde lipid transport.
419 *eLife*. **9**, e56571

420 22. Simons, K. T., Bonneau, R., Ruczinski, I., and Baker, D. (1999) Ab initio
421 protein structure prediction of CASP III targets using ROSETTA. *Proteins Struct.*
422 *Funct. Bioinforma.* **37**, 171–176

423 23. Pettersen, E. F., Goddard, T. D., Huang, C. C., Couch, G. S., Greenblatt, D.
424 M., Meng, E. C., and Ferrin, T. E. (2004) UCSF Chimera--a visualization system for
425 exploratory research and analysis. *J. Comput. Chem.* **25**, 1605–1612

426 24. Song, Y., DiMaio, F., Wang, R. Y.-R., Kim, D., Miles, C., Brunette, T.,
427 Thompson, J., and Baker, D. (2013) High resolution comparative modeling with
428 RosettaCM. *Struct. Lond. Engl. 1993*. 10.1016/j.str.2013.08.005

429 25. O'Boyle, N. M., Banck, M., James, C. A., Morley, C., Vandermeersch, T., and
430 Hutchison, G. R. (2011) Open Babel: An open chemical toolbox. *J. Cheminformatics*.
431 **3**, 33

432 26. Wang, J., Wang, W., Kollman, P. A., and Case, D. A. (2006) Automatic atom
433 type and bond type perception in molecular mechanical calculations. *J. Mol. Graph.*
434 *Model.* **25**, 247–260

435 27. Šali, A., and Blundell, T. L. (1993) Comparative Protein Modelling by
436 Satisfaction of Spatial Restraints. *J. Mol. Biol.* **234**, 779–815

437 28. Sánchez, R., and Šali, A. (2000) Comparative Protein Structure Modeling:
438 Introduction and Practical Examples with Modeller. in *Protein Structure Prediction*,
439 pp. 97–129, Humana Press, New Jersey, 10.1385/1-59259-368-2:97

440 29. Jo, S., Kim, T., Iyer, V. G., and Im, W. (2008) CHARMM-GUI: A web-based
441 graphical user interface for CHARMM. *J. Comput. Chem.* **29**, 1859–1865

442 30. Brooks, B. R., Brooks, C. L., Mackerell, A. D., Nilsson, L., Petrella, R. J., Roux,
443 B., Won, Y., Archontis, G., Bartels, C., Boresch, S., Caflisch, A., Caves, L., Cui, Q.,
444 Dinner, A. R., Feig, M., Fischer, S., Gao, J., Hodoscek, M., Im, W., Kuczera, K.,
445 Lazaridis, T., Ma, J., Ovchinnikov, V., Paci, E., Pastor, R. W., Post, C. B., Pu, J. Z.,
446 Schaefer, M., Tidor, B., Venable, R. M., Woodcock, H. L., Wu, X., Yang, W., York, D.
447 M., and Karplus, M. (2009) CHARMM: The biomolecular simulation program. *J.*
448 *Comput. Chem.* **30**, 1545–1614

449 31. Lee, J., Cheng, X., Swails, J. M., Yeom, M. S., Eastman, P. K., Lemkul, J. A.,
450 Wei, S., Buckner, J., Jeong, J. C., Qi, Y., Jo, S., Pande, V. S., Case, D. A., Brooks,
451 C. L., MacKerell, A. D., Klauda, J. B., and Im, W. (2016) CHARMM-GUI Input
452 Generator for NAMD, GROMACS, AMBER, OpenMM, and CHARMM/OpenMM
453 Simulations Using the CHARMM36 Additive Force Field. *J. Chem. Theory Comput.*
454 **12**, 405–413

455 32. Wu, E. L., Cheng, X., Jo, S., Rui, H., Song, K. C., Dávila-Contreras, E. M., Qi,
456 Y., Lee, J., Monje-Galvan, V., Venable, R. M., Klauda, J. B., and Im, W. (2014)
457 CHARMM-GUI *Membrane Builder* toward realistic biological membrane simulations.
458 *J. Comput. Chem.* **35**, 1997–2004

459 33. Jo, S., Lim, J. B., Klauda, J. B., and Im, W. (2009) CHARMM-GUI membrane
460 builder for mixed bilayers and its application to yeast membranes. *Biophys. J.* **97**, 50–
461 58

462 34. Jo, S., Kim, T., and Im, W. (2007) Automated Builder and Database of
463 Protein/Membrane Complexes for Molecular Dynamics Simulations. *PLoS ONE*. **2**,
464 e880

465 35. Lee, J., Patel, D. S., Ståhle, J., Park, S. J., Kern, N. R., Kim, S., Lee, J.,
466 Cheng, X., Valvano, M. A., Holst, O., Knirel, Y. A., Qi, Y., Jo, S., Klauda, J. B.,
467 Widmalm, G., and Im, W. (2019) CHARMM-GUI Membrane Builder for Complex
468 Biological Membrane Simulations with Glycolipids and Lipoglycans. *J. Chem. Theory*
469 *Comput.* **15**, 775–786

470 36. Holdbrook, D. A., Huber, R. G., Piggot, T. J., Bond, P. J., and Khalid, S. (2016)

Dynamics of Crowded Vesicles: Local and Global Responses to Membrane Composition. *PLOS ONE*. **11**, e0156963

37. Humphrey, W., Dalke, A., and Schulten, K. (1996) VMD: visual molecular dynamics. *J. Mol. Graph.* **14**, 33–8, 27–8

38. Van Der Spoel, D., Lindahl, E., Hess, B., Groenhof, G., Mark, A. E., and Berendsen, H. J. C. (2005) GROMACS: Fast, flexible, and free. *J. Comput. Chem.* **26**, 1701–1718

39. Huang, J., and MacKerell, A. D. (2013) CHARMM36 all-atom additive protein force field: Validation based on comparison to NMR data. *J. Comput. Chem.* **34**, 2135–2145

40. Essmann, U., Perera, L., Berkowitz, M. L., Darden, T., Lee, H., and Pedersen, L. G. (1995) A smooth particle mesh Ewald method. *J. Chem. Phys.* **103**, 8577–8593

41. Hess, B., Bekker, H., Berendsen, H. J. C., and Fraaije, J. G. E. M. (1997) LINCS: A linear constraint solver for molecular simulations. *J. Comput. Chem.* **18**, 1463–1472

42. Hoover, W. G. (1985) *Canonical dynamics: Equilibrium phase-space distributions*

43. Nosé, S. (1984) A molecular dynamics method for simulations in the canonical ensemble. *Mol. Phys.* **52**, 255–268

44. Parrinello, M., and Rahman, A. (1981) Polymorphic transitions in single crystals: A new molecular dynamics method. *J. Appl. Phys.* **52**, 7182–7190

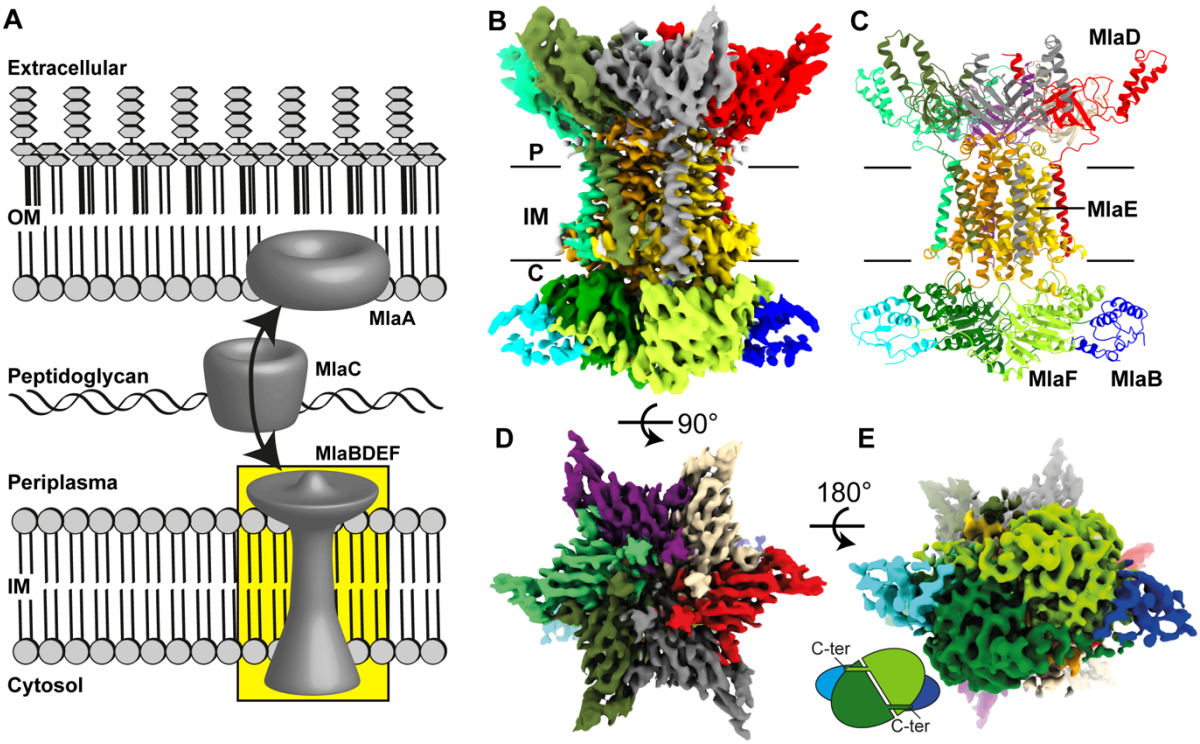

493

494 **Figure 1: Structure of MlaBDEF$_{ab}$** A: Scheme of lipid transport by the MlaABCDEF
495 system in gram-negative bacteria (OM = outer membrane; IM = inner membrane). B:
496 3.9 Å CryoEM map of MlaBDEF$_{ab}$-AppNHp in DDM (C=cytosol, IM=inner membrane,
497 P=periplasma). C: MlaBDEF$_{ab}$ has global C2 symmetry with six copies of MlaD that
498 span the inner membrane from the periplasmic space to the cytosol, two copies of
499 MlaE embedded in the membrane (yellow/gold), two copies of the ATPase MlaF in the
500 cytosol (green), each bound to a copy of MlaB (blue/cyan). D: top view of the
501 MlaBDEF$_{ab}$ complex reveals C6 symmetry of MlaD. E: C-terminal regions of MlaF bind
502 the opposing MlaB subunit via a “handshake-mechanism”.

503

504

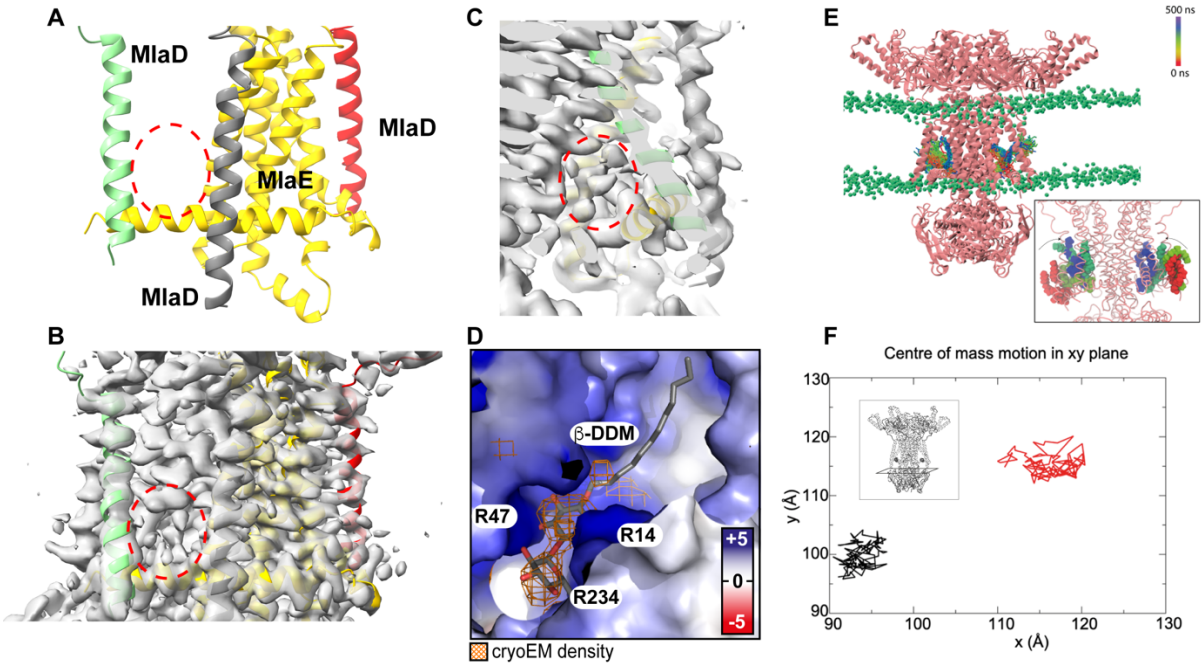

Figure 2: Detergent position and dynamics at the MlaD TM-MlaE interface. A-C: Transmembrane region of MlaBDEF$_{ab}$ with one MlaE and three MlaD proteins shown. Red circles indicates density unoccupied by protein residues. D: Electrostatic surface potential of modeled inner membrane MlaBDEF$_{ab}$ (blue=+5 kT/e, white=0kT/e, red=-5kT/e) shows a cationic binding site for anionic lipid head groups like □-DDM and an apolar pocket for the uncharged lipid tails. □-DDM was modeled inside the previously empty CryoEM density (orange). E-F: Molecular dynamics simulations show spontaneous, stable binding of lipids into the cytosolic binding pockets of MlaBDEF. Lipid-free MlaBDEF$_{ab}$ was embedded into an inner membrane model system of 75% POPE, 20% POPG, 5% Cardiolipin (Methods section for details). Panel E shows the location of two POPE lipids during a 500 ns simulation, the colour scheme indicates the movement of the lipids as shown in the legend. In this simulation the lipids moved into this location spontaneously during the equilibration process, as shown in the close-up view in the inset in which the red coloured lipids indicate starting positions before the equilibration process. Panel F shows the motion of the lipids in the xy plane (inset) over 500 ns. The lipids are confined within an area of 10 x 10 Å for 500 ns, showing this location is favourable.

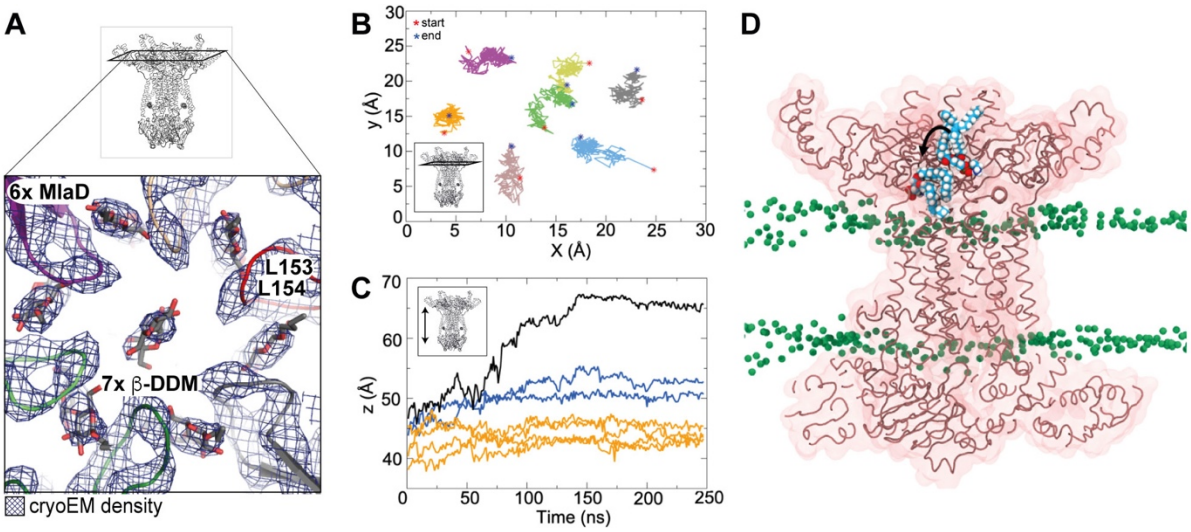

Figure 3: Lipid position and dynamics in the MlaD basket. A: Close-up of the periplasmic MlaD basket that houses six peripheral and one central detergent molecule. B-D: Spontaneous lipid flipping within the basket region of $MlaBDEF_{ab}$ during 250 ns molecular dynamics simulations. Panel B shows the center of mass motion of the seven lipids in the xy plane. They are confined to an area of ~5 x 5 Å, indicating this is a high lipid affinity region. Panel C shows the center of mass movement of the seven lipids in the Z dimension as a function of time. The higher values of z correspond to the cytoplasmic end of the protein. The lipid shown in panel A corresponds to the black curve showing a clear movement towards the cytoplasmic end. Three other lipids (blue) move into this channel but to a lesser extent than the aforementioned lipid, whereas three others (orange) remain close to their starting positions. Simulations from a model at the reported resolution cannot clarify the directionality of the movement, but rather that these regions are conduits for lipids. Panel D shows a cut-away view of the protein with a POPE lipid at two time points during the simulation, time = 0 ns and 150 ns. The simulation was initiated with seven POPE lipids placed at the periplasmic end of the protein corresponding to the density for detergents in the cryo-EM data (Table S2). The lipid which is displaced more towards the cytoplasmic end is from the frame at t = 150 ns. The central hydrophobic 'channel' of the protein is a clear conduit for lipids given the spontaneous movement of POPE into this region in just 150 ns.

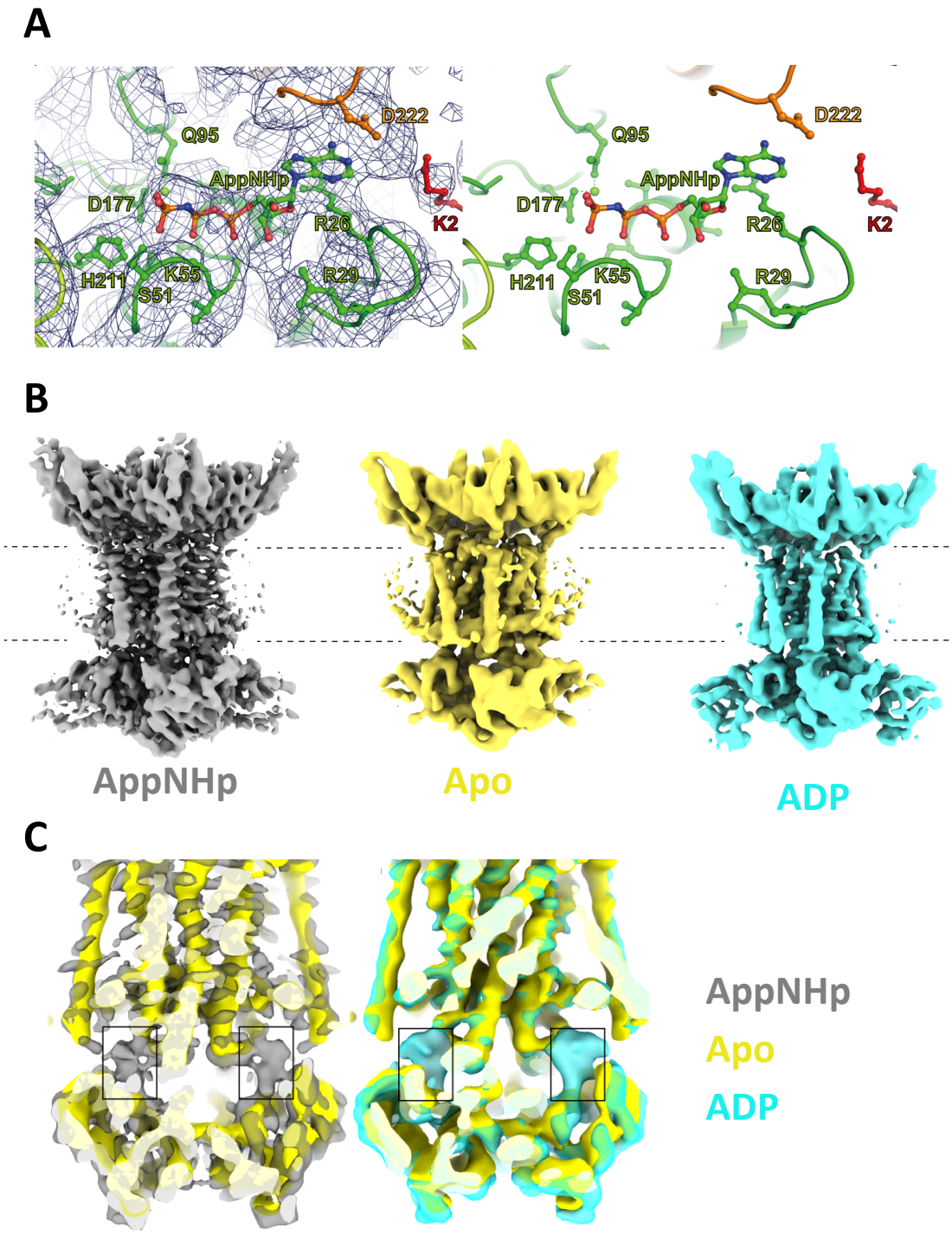

548

549 **Figure 4: Nucleotide position in the MlaBDEF$_{ab}$ structure.** (A) AppNHp is bound at
550 the interface of MlaE (orange), MlaD (red) and MlaF (green). B: maps of MlaBDEF$_{ab}$
551 bound to AppNHp (grey), its *apo* state (yellow) and bound to ADP (cyan). (C) The
552 overlay of the maps unambiguously confirms the presence of nucleotide in the AppNHp
553 and ADP maps, but not in the Apo map. Nonetheless, no overall structural changes is
554 observed.

555

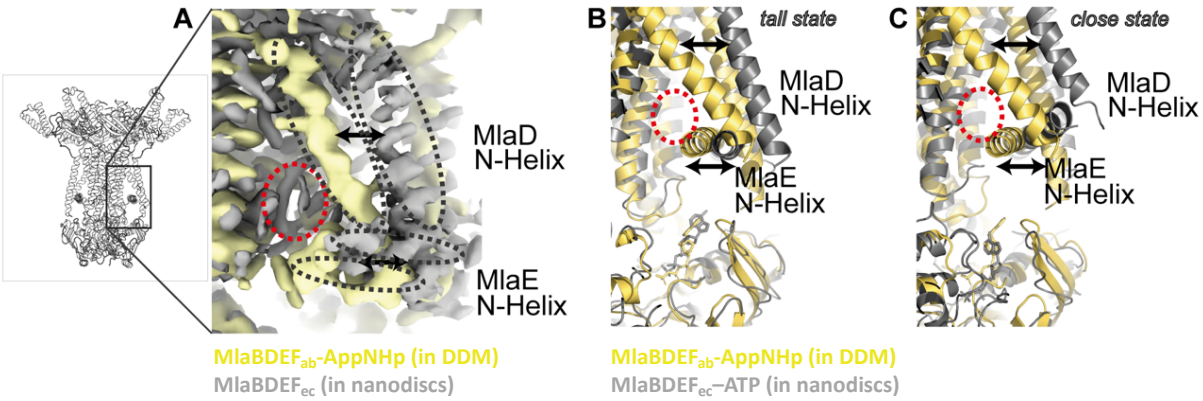

Figure 5: Comparison of the MlaBDEF$_{ab}$ and MlaBDEF$_{ec}$ structures. Acquired Cryo-EM map of MlaBDEF$_{ec}$ in lipid nanodiscs (20) and MlaBDEF$_{ab}$ in a DDM micelle (this study) show large differences in the lower lipid binding sites. A: Both the MlaD N-terminal helix and the MlaE N-terminal helix form a much smaller lipid binding pocket (red circle) in detergent environment (yellow, this study) compared to lipid environment (grey, EMD-30355). Two nucleotide binding states were observed in the MlaBDEF$_{ec}$ study; “tall” and “close”. Comparison to B) “tall state” (grey) shows almost identical nucleotide position between MlaBDEF$_{ec}$ and MlaBDEF$_{ab}$, whereas

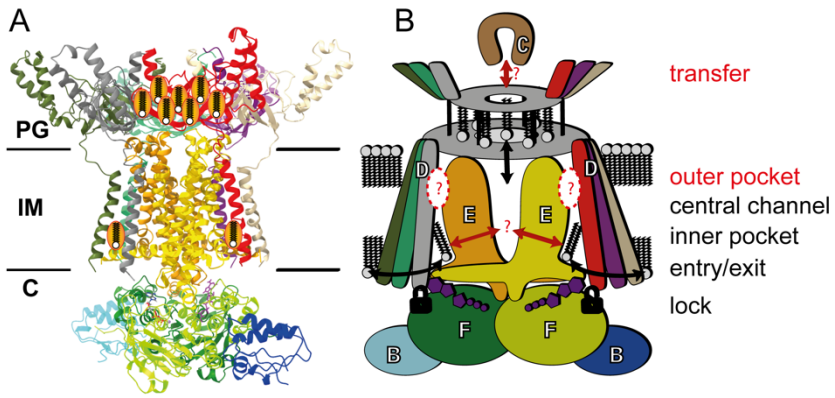

Figure 6: Molecular model of lipid transport by the MlaBDEF complex. A: structural model and B: observed degrees of freedom in this study. Lipids can move freely into the cytosolic paired binding pockets ("entry/exit") that are very close to the ATP binding sites that directly bind MlaD ("lock"). Lipids can move and even flip inside the basket region ("transport"). C: The elucidated structures could not show how transport from the entry sites to the basket region is performed and how lipid exchange to/from MlaC is achieved.

576 **Table 1: Cryo-EM data processing and refinement statistics**

	AppNHp (EMDB-11082 (PDB: 6Z5U)	**Apo** (EMDB-11083)	**ADP** (EMDB-11084)
Data Collection and Processing			
Microscope	Titan Krios	Titan Krios	Titan Krios
Voltage (kV)	300	300	300
Camera	K2 summit	K3 bioquantum	K2 summit
Pixel size (Å)	1.07	0.41	1.07
Defocus range (μm)	-1 to -2.5	-0.8 to -2.0	-1 to -2.5
Total dose (eÅ^{-2})	47	40	40
Number of micrographs	2557	4737	1901
Total particles used	93,295	28,699	62,512
Map Resolution (Å)	3.92	4.24	4.43
Refinement			
Model composition			
Non-hydrogen atoms	17,892		
Protein Residues	2334		
Ligand atoms	4		
B factors (Å^{-1})			
Protein	145.24		
Ligand	170.31		
R.m.s. deviations			
Bond lengths (Å)	0.008		
Bond angles (°)	1.384		
Validation			
MolProbity score	3.43		
Clashscore	35.15		
Poor rotamers (%)	10.94		
Ramachandran plot			
Favoured (%)	87.45		
Allowed (%)	10.94		
Disallowed (%)	0.43		

577